

# Free-carrier electro-refraction modulation based on a silicon slot waveguide with ITO

Junsu Baek, Jong-Bum You, and Kyoungsik Yu\*

Department of Electrical Engineering, KAIST, Daejeon, South Korea

\*ksyu@kaist.edu

**Abstract:** Recently, silicon-waveguide-based hybrid modulators with high-performance electro-optic materials have been proposed to overcome the intrinsic limitations of silicon materials. Indium-tin-oxide (ITO) is one of the important candidates for such applications due to its unique features including the ENZ effect and electrically tunable permittivity. In this paper, we propose an ultra-compact integrated phase modulator which consists of a silicon slot waveguide with a thin ITO film in the slot region. In the near-infrared regime, bias-voltage-dependent free-carrier accumulation at the dielectric-ITO interface induces an epsilon-near-zero (ENZ) effect, and contributes to the strong phase modulation of the guided electromagnetic wave. With a voltage swing of 2 V, the device experiences a large variation of the effective modal index, resulting in a  $\pi$  radian phase shift within the device length of  $<5 \mu\text{m}$  at 210 THz according to our computer simulations. A high modulation efficiency of  $V_{\pi}L_{\pi} \sim 0.0071 \text{ V}\cdot\text{cm}$  and a large device bandwidth of  $\sim 70 \text{ GHz}$  suggest a potential for an ultra-compact optoelectronic component in the integrated silicon photonics platform.

©2015 Optical Society of America

**OCIS codes:** (250.4110) Modulators; (250.7360) Waveguide modulators; (160.2100) Electro-optical materials.

---

## References and links

1. D. A. B. Miller, "Device requirements for optical interconnects to silicon chips," *Proc. IEEE* **97**(7), 1166–1185 (2009).
2. M. Asghari and A. V. Krishnamoorthy, "Silicon photonics: energy-efficient communication," *Nat. Photonics* **5**(5), 268–270 (2011).
3. F. Gardes, G. Reed, N. Emerson, and C. Png, "A sub-micron depletion-type photonic modulator in silicon on insulator," *Opt. Express* **13**(22), 8845–8854 (2005).
4. A. Liu, L. Liao, D. Rubin, H. Nguyen, B. Ciftcioglu, Y. Chetrit, N. Izhaky, and M. Paniccia, "High-speed optical modulation based on carrier depletion in a silicon waveguide," *Opt. Express* **15**(2), 660–668 (2007).
5. W. M. Green, M. J. Rooks, L. Sekaric, and Y. A. Vlasov, "Ultra-compact, low RF power, 10 Gb/s silicon Mach-Zehnder modulator," *Opt. Express* **15**(25), 17106–17113 (2007).
6. J. H. Wülbern, S. Prorok, J. Hampe, A. Petrov, M. Eich, J. Luo, A. K.-Y. Jen, M. Jenett, and A. Jacob, "40 GHz electro-optic modulation in hybrid silicon-organic slotted photonic crystal waveguides," *Opt. Lett.* **35**(16), 2753–2755 (2010).
7. S. Koeber, R. Palmer, M. Lauermann, W. Heni, D. L. Elder, D. Korn, M. Woessner, L. Alloatti, S. Koenig, and P. C. Schindler, "Femtojoule electro-optic modulation using a silicon-organic hybrid device," *Light Sci. Appl.* (2014).
8. H. Gomes, P. Stallinga, M. Cölle, D. De Leeuw, and F. Biscarini, "Electrical instabilities in organic semiconductors caused by trapped supercooled water," *Appl. Phys. Lett.* **88**(8), 082101 (2006).
9. F. Michelotti, L. Dominici, E. Descrovi, N. Danz, and F. Menchini, "Thickness dependence of surface plasmon polariton dispersion in transparent conducting oxide films at  $1.55 \mu\text{m}$ ," *Opt. Lett.* **34**(6), 839–841 (2009).
10. M. Noginov, L. Gu, J. Livenere, G. Zhu, A. Pradhan, R. Mundle, M. Bahoura, Y. A. Barnakov, and V. Podolskiy, "Transparent conductive oxides: plasmonic materials for telecom wavelengths," *Appl. Phys. Lett.* **99**(2), 021101 (2011).
11. D. Traviss, R. Bruck, B. Mills, M. Abb, and O. L. Muskens, "Ultrafast plasmonics using transparent conductive oxide hybrids in the epsilon-near-zero regime," *Appl. Phys. Lett.* **102**(12), 121112 (2013).
12. H. Zhao, Y. Wang, A. Capretti, L. Dal Negro, and J. Klamkin, "Broadband electroabsorption modulators design based on epsilon-near-zero indium tin oxide," *IEEE J. Sel. Top. Quantum Electron.* **21**(4), 3300207 (2015).

13. A. Melikyan, N. Lindenmann, S. Walheim, P. M. Leufke, S. Ulrich, J. Ye, P. Vincze, H. Hahn, T. Schimmel, C. Koos, W. Freude, and J. Leuthold, "Surface plasmon polariton absorption modulator," *Opt. Express* **19**(9), 8855–8869 (2011).
14. Z. Lu, W. Zhao, and K. Shi, "Ultracompact electroabsorption modulators based on tunable epsilon-near-zero-slot waveguides," *IEEE Photonics J.* **4**(3), 735–740 (2012).
15. A. P. Vasudev, J.-H. Kang, J. Park, X. Liu, and M. L. Brongersma, "Electro-optical modulation of a silicon waveguide with an "epsilon-near-zero" material," *Opt. Express* **21**(22), 26387–26397 (2013).
16. S. Zhu, G. Q. Lo, and D. L. Kwong, "Design of an ultra-compact electro-absorption modulator comprised of a deposited TiN/HfO<sub>2</sub>/ITO/Cu stack for CMOS backend integration," *Opt. Express* **22**(15), 17930–17947 (2014).
17. H. W. Lee, G. Papadakis, S. P. Burgos, K. Chander, A. Kriesch, R. Pala, U. Peschel, and H. A. Atwater, "Nanoscale conducting oxide PlasMOStor," *Nano Lett.* **14**(11), 6463–6468 (2014).
18. A. V. Krasavin and A. V. Zayats, "Photonic signal processing on electronic scales: electro-optical field-effect nanoplasmonic modulator," *Phys. Rev. Lett.* **109**(5), 053901 (2012).
19. K. Shi, W. Zhao, and Z. Lu, "Epsilon-near-zero-slot waveguides and their applications in ultrafast laser beam steering," in *SPIE OPTO*, (International Society for Optics and Photonics, 2014), 89800L–89800L–89807.
20. D. Ly-Gagnon, S. Tsukamoto, K. Katoh, and K. Kikuchi, "Coherent detection of optical quadrature phase-shift keying signals with carrier phase estimation," *J. Lightwave Technol.* **24**(1), 12–21 (2006).
21. P. Dong, C. Xie, L. Chen, N. K. Fontaine, and Y. K. Chen, "Experimental demonstration of microring quadrature phase-shift keying modulators," *Opt. Lett.* **37**(7), 1178–1180 (2012).
22. J. W. Elam, D. A. Baker, A. B. Martinson, M. J. Pellin, and J. T. Hupp, "Atomic layer deposition of indium tin oxide thin films using nonhalogenated precursors," *J. Phys. Chem. C Nanomater. Interfaces* **112**, 1938–1945 (2008).
23. S. Govindarajan, T. Boscke, P. Sivasubramani, P. Kirsch, B. Lee, H.-H. Tseng, R. Jammy, U. Schroder, S. Ramanathan, and B. Gnade, "Higher permittivity rare earth doped HfO<sub>2</sub> for sub-45-nm metal-insulator-semiconductor devices," *Appl. Phys. Lett.* **91**, 062906–062906–062903 (2007).
24. H. Kim, P. C. McIntyre, and K. C. Saraswat, "Effects of crystallization on the electrical properties of ultrathin HfO<sub>2</sub> dielectrics grown by atomic layer deposition," *Appl. Phys. Lett.* **82**(1), 106–108 (2003).
25. TCAD, Silvaco Inc. (2014), <http://www.silvaco.com>.
26. Y. Park, V. Choong, Y. Gao, B. Hsieh, and C. Tang, "Work function of indium tin oxide transparent conductor measured by photoelectron spectroscopy," *Appl. Phys. Lett.* **68**(19), 2699–2701 (1996).
27. S. Ishibashi, Y. Higuchi, Y. Ota, and K. Nakamura, "Low resistivity indium–tin oxide transparent conductive films. II. effect of sputtering voltage on electrical property of films," *J. Vac. Sci. Technol. A* **8**(3), 1403–1406 (1990).
28. H. Kim, A. Pique, J. Horwitz, H. Mattoussi, H. Murata, Z. Kafafi, and D. Chrisey, "Indium tin oxide thin films for organic light-emitting devices," *Appl. Phys. Lett.* **74**(23), 3444–3446 (1999).
29. Y. J. Kim, S. B. Jin, S. I. Kim, Y. S. Choi, I. S. Choi, and J. G. Han, "Study on the electrical properties of ITO films deposited by facing target sputter deposition," *J. Phys. D Appl. Phys.* **42**(7), 075412 (2009).
30. F. Neumann, Y. A. Genenko, C. Melzer, S. Yamolskii, and H. von Seggern, "Self-consistent analytical solution of a problem of charge-carrier injection at a conductor/insulator interface," *Phys. Rev. B Condens. Matter* **75**(20), 205322 (2007).
31. B. H. Lee, R. Choi, L. Kang, S. Gopalan, R. Nieh, K. Onishi, Y. Jeon, W.-J. Qi, C. Kang, and J. Lee, "Characteristics of TaN gate MOSFET with ultrathin hafnium oxide," in *Electron Devices Meeting, 2000. IEDM'00. Technical Digest. International*, (IEEE, 2000), 39–42.
32. E. Feigenbaum, K. Diest, and H. A. Atwater, "Unity-order index change in transparent conducting oxides at visible frequencies," *Nano Lett.* **10**(6), 2111–2116 (2010).
33. C. O. M. S. O. L. Multiphysics, Version 5.0 Comsol Inc. (2014), <http://www.comsol.com>.
34. R. F. Oulton, V. J. Sorger, D. Genov, D. Pile, and X. Zhang, "A hybrid plasmonic waveguide for subwavelength confinement and long-range propagation," *Nat. Photonics* **2**(8), 496–500 (2008).
35. C.-L. Zou, F.-W. Sun, Y.-F. Xiao, C.-H. Dong, X.-D. Chen, J.-M. Cui, Q. Gong, Z.-F. Han, and G.-C. Guo, "Plasmon modes of silver nanowire on a silica substrate," *Appl. Phys. Lett.* **97**(18), 183102 (2010).
36. K. Padmaraju, N. Ophir, Q. Xu, B. Schmidt, J. Shaky, S. Manipatruni, M. Lipson, and K. Bergman, "Error-free transmission of microring-modulated BPSK," *Opt. Express* **20**(8), 8681–8688 (2012).
37. D. Feng, S. Liao, H. Liang, J. Fong, B. Bijlani, R. Shafiqi, B. J. Luff, Y. Luo, J. Cunningham, A. V. Krishnamoorthy, and M. Asghari, "High speed GeSi electro-absorption modulator at 1550 nm wavelength on SOI waveguide," *Opt. Express* **20**(20), 22224–22232 (2012).

## 1. Introduction

As the demands for high-speed and large-bandwidth information processing increase, the major performance bottleneck has shifted to communications/interconnections between the integrated circuit modules, and the optical interconnects are considered as one of the most preferable technologies for the wide bandwidth data transmission [1]. Especially, silicon photonics has attracted a lot of interest in the miniaturization and integration of electro-optic devices, such as amplitude/phase modulators and switches for ultrafast and energy-efficient

optical signal processing, because of its high modal confinement and low absorption losses at near-infrared wavelengths due to the silicon's large refractive index [2]. The silicon material has a number of advantages over other semiconductor materials because of its mature fabrication processes and availability for chip-scale integration.

Since there are no second-order nonlinearities in silicon, a common way to affect its refractive index for high-speed optical modulation is to inject or deplete the free carriers, resulting in a change of electron and hole densities. Typical silicon-based electro-optic modulators employ a reverse-biased p-n junction, and rely on the electric-field driven carrier dynamics. Such an approach can achieve high operation speed up to  $\sim 30$  Gb/s because the response time can be shorter than 10 ps [3]. However, the device requires a very long phase modulation length over 1 mm, which might not be suitable for the future high-density optical circuits [4]. On the other hand, the silicon modulators based on forward-biased p-i-n diodes have relatively high modulation efficiency of  $V_{\pi}L_{\pi} \sim 0.04$  V·cm, but they usually suffer from low modulation speeds when special driving techniques, such as pre-emphasis, are not employed [5]. In addition, their energy efficiency is also restricted due to the permanent injection current. The fundamental trade-off between the modulation efficiency and the operational speed is mainly due to the intrinsic limitations of the silicon materials and difficult to overcome with all-silicon approaches.

To overcome the disadvantages of the silicon devices, the so-called hybrid modulators using silicon waveguide-based structures with other electro-optic materials have been proposed. Silicon-organic hybrid (SOH) modulators have been demonstrated by combining silicon-on-insulator (SOI) slot waveguides with organic cladding films [6, 7]. The SOH devices have merits in terms of a broad range of operation wavelengths and a large modulation bandwidth. However, it is difficult to design appropriate electro-optic organic materials due to the severe electrical instabilities [8]. Another important candidate is indium tin oxide (ITO). The ITO permittivity in the optical wavelengths can be typically approximated with the Drude model [9, 10], and an ENZ regime occurs near a near-infrared wavelength depending on its free carriers concentrations [11, 12]. The unique features of the ENZ effect and electrically tunable permittivity ensure the ITO thin film to be used as a high-performance electro-optic material in silicon photonics platform. Several waveguide-based modulators overcoated with the combination of dielectric and ITO layers have been suggested and demonstrated. Melikyan *et. al* has experimentally demonstrated an ITO plasmonic absorption modulator [13]. Due to a small change of a free carrier density ratio in the ITO film, the device has a low extinction ratio (ER) of  $\sim 1.5$ , but the modulator itself has shown the feasibility as a novel absorption modulation scheme based on voltage-tunable permittivities. After that, some research papers have theoretically suggested that ITO's ENZ property can induce a large absorption coefficient difference between an 'on' and 'off' state [12, 14–16]. Especially, slot waveguide absorption modulators with an ITO core have shown extremely high ERs in their theoretical calculation [12, 14]. Afterwards, it was experimentally proven that the ENZ effect can indeed dramatically affect the modulation efficiency [17]. According to the experiments [17], high ER ( $\sim 2.71$  dB/ $\mu\text{m}$ ) and low insertion loss ( $\sim 0.45$  dB/ $\mu\text{m}$ ) have been simultaneously achieved.

In addition to absorption modulation, there also have been efforts on designing phase modulators based on the ITO material. An active electro-optical field-effect nanoplasmonic modulator has been numerically demonstrated and has shown changes of an effective refractive index as well as an effective extinction coefficient depending on voltage biases for phase modulation [18]. However, it also has indicated that only a small portion of the effective refractive index is changed when compared to the absorption coefficient in the device. A beam steering device has been proposed based on slot waveguide phase modulators with ITO [19]. By taking advantages of the ENZ effect, about  $60^\circ$  steering angle is achieved on the silicon grating surface.

In this paper, we propose an integrated ultra-compact phase modulator which consists of a silicon slot waveguide with a thin ITO film in the slot region. Due to the combination of high and low-index layers, the slot waveguide can tightly confine the electro-magnetic field into the active region of ITO. By applying a certain voltage bias between the ITO and doped silicon layers, both the propagation constant and absorption coefficient of the fundamental transverse magnetic-like (TM) mode dramatically change, resulting in both the phase and amplitude modulation. Together with the amplitude modulation, efficient phase modulation techniques are important for a number of applications, such as optical quadrature phase-shift keying for high-speed digital communication [20, 21].

The paper is organized as follows. Section 2 is a brief introduction of our device structure. Section 3 investigates the dispersion relation of ITO and the free carrier concentration of the active region in the modulator. In Section 4, we show the feasibility of phase modulation by analyzing the TM mode propagation characteristics with respect to the operation frequencies and bias voltages. Section 5 investigates the device performance in terms of the coupling efficiency, energy consumption, and switching speed. Section 6 is the conclusion.

## 2. Device structure

A schematic illustration of our electro-optical amplitude/phase modulator is shown in Fig. 1(a). It consists of a vertically-stacked silicon slot waveguide on the SOI wafer. The ITO layer can be considered as a degenerate semiconductor with a large number of electrons, and the film can be conformably deposited on the silicon waveguide by an atomic layer deposition (ALD) process [22]. We choose  $\text{HfO}_2$  as a dielectric material because of its high static permittivity ( $\epsilon_{\text{HfO}_2} = \sim 25$ ) [23]. In addition, the thin film can be reliably grown by using the ALD technique to tolerate high electric field induced with relatively low voltage biases [24]. The surrounding material over the waveguide is the uniform silicon dioxide. We assume that a fundamental TM mode light is launched from the silicon rib waveguide in Fig. 1(b) so that it has good overlap with the active region of the ITO layer.

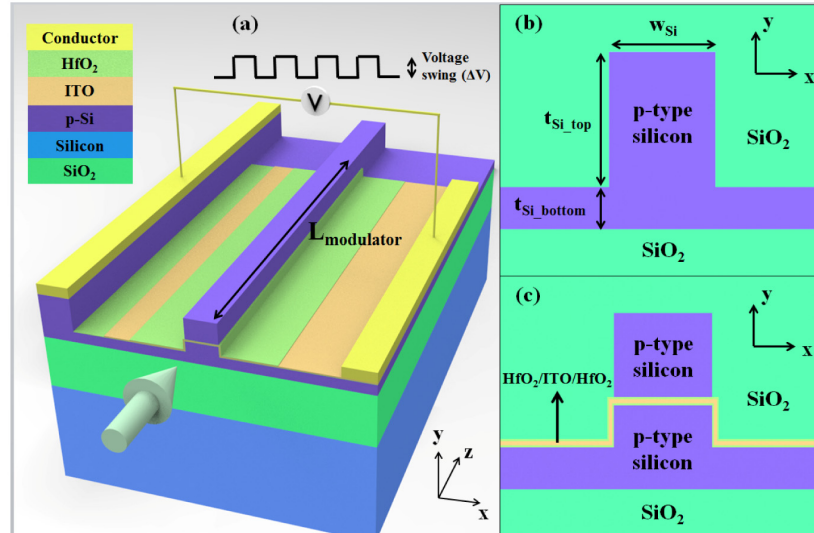


Fig. 1. (a) The schematic diagram of the proposed electro-optical modulator. The guided TM mode input light (green arrow) is launched into the silicon waveguide. Due to the refractive index difference between the core materials (ITO and  $\text{HfO}_2$ ) and silicon, the electro-magnetic field can be confined in the active material (ITO).  $\Delta V$  is a voltage swing applied to the device.  $L_{\text{modulator}}$  is a total length of the modulator. (b) Cross-section of the silicon rib waveguide before and after the modulator section. ( $w_{\text{Si}} = 300$  nm,  $t_{\text{Si\_top}} = 320$  nm, and  $t_{\text{Si\_bottom}} = 100$  nm) (c) Cross-section of the slot waveguide modulator.

The input and output facet of the waveguide modulator with an ITO core layer are connected to the conventional silicon rib waveguide as shown in the Figs. 1(b)-1(c). An AC voltage source with a constant offset ( $V_{dc}$ ) and a voltage swing ( $\Delta V$ ) is connected between the ITO and p-type silicon (see Fig. 2(a) for details). We assume that the external electrodes form ohmic contacts with ITO and p-type Si. When a negative voltage bias is applied to the ITO gate, a large number of free carriers are accumulated in the interface between the dielectric and ITO layer. The optical property of the active material therefore changes dramatically, resulting in strong optical modulation effects. When compared to a single metal-oxide-semiconductor (MOS) structure [14], the proposed modulator consists of two MOS stacks which are connected in parallel to each other. Since two electron-accumulated layers are formed at the dielectric-ITO interfaces, the thickness of the active region becomes twice. As a result, the electro-optic effect increases considerably. The operation mechanism of the proposed structure with two MOS stacks is similar to a previously reported absorption modulator structure with an Au/Al<sub>2</sub>O<sub>3</sub>/ITO/Al<sub>2</sub>O<sub>3</sub>/Au stack [17].

### 3. Electro-optical effect in the modulator

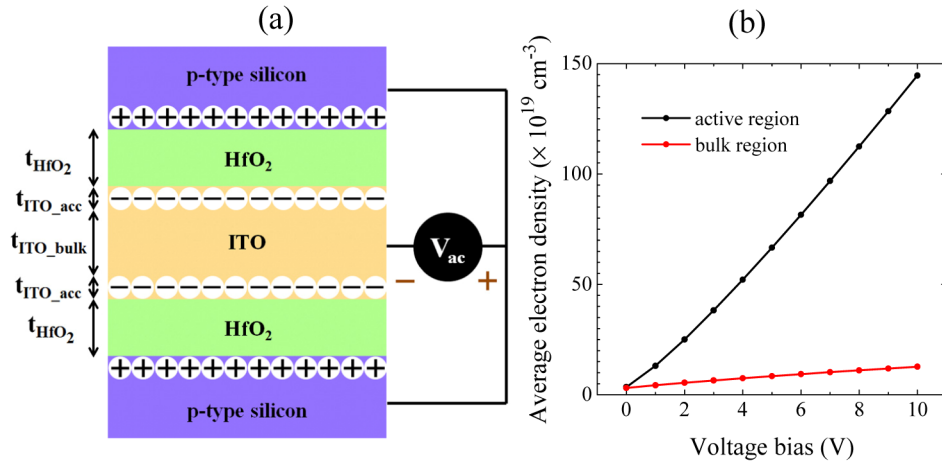


Fig. 2. (a) A simplified schematic diagram for the electrical simulation. ( $t_{\text{ITO}} = 2t_{\text{ITO\_acc}} + t_{\text{ITO\_bulk}} = 10 \text{ nm}$ ,  $t_{\text{HfO}_2} = 5 \text{ nm}$ ) (b) Average free carrier density in the accumulation (black curve) and bulk (red curve) region of the ITO layer. The accumulation length,  $t_{\text{ITO\_acc}}$ , approximated by the Thomas-Fermi screening effect, is  $\sim 1 \text{ nm}$ . The bulk length,  $t_{\text{ITO\_bulk}}$ , is  $\sim 8 \text{ nm}$ .

To analyze the electro-optic modulation effect, we first need to find the change of free carrier densities at the ITO-HfO<sub>2</sub> interface with respect to the input voltage. For electrical simulation, the modulator is simplified to a 2D structure model as shown in Fig. 2(a). A commercial software [25] is used to calculate the carrier distributions in a highly doped semiconductor with a high electric field. Fermi-Dirac statistics, bandgap narrowing, doping-dependent mobility, and electric-field-dependent mobility model are also considered. Table 1 summarizes the electrical simulation parameters for ITO.

Table 1. Simulation parameters for the electrical properties of an indium-tin-oxide thin film

Doping concentration ( $N_D$ )	$3 \times 10^{19} \text{ cm}^{-3}$
Work function ( $\Phi$ )	4.4 eV [26]
Electrical resistivity ( $\rho_{\text{ITO}}$ )	$5 \times 10^{-4} \Omega \cdot \text{cm}$ [27]
Bandgap at 300K ( $E_g$ )	3.8 eV [28]
Hall mobility ( $\mu_{\text{Hall}}$ )	$40 \text{ cm}^2 \cdot \text{V}^{-1} \cdot \text{s}^{-1}$ [29]
Relative electrical permittivity ( $\epsilon_{\text{ITO}}$ )	9.8 [30]

When the voltage bias is applied to the device as shown in Fig. 2(a), electrons are accumulated near the dielectric interface, and the ITO layer can be approximately divided into two parts: bulk and accumulation region. The accumulation layer thickness in the typical MOS structure is only ~1 nm when the effects of electric field screening by electron carriers are considered, and given by the Thomas-Fermi screening length [13, 18],

$$t_{ITO\_acc} = \lambda_{TF} = \left( \frac{\epsilon_{ITO} \epsilon_0 h^2}{4\pi^2 m_{eff} e^2} \right)^{1/2} \left( \frac{\pi^4}{3N_0} \right)^{1/6}, \quad (1)$$

where  $m_{eff}$  is the effective mass of an electron,  $h$  is a Plank constant, and  $\epsilon_0$  is the vacuum permittivity. The effective electron mass of the ITO is obtained from Neumann *et. al* ( $m_{eff} = 0.35 \times m_{electron}$ ) [30]. Based on the effects of electric field screening by electrons in solid, Eq. (1) gives an approximation of electron distribution length at the metallic surface. From the simulation results, we plot the electron concentration with respect to the voltage bias in Fig. 2(b). Notice that a larger voltage bias induces more free-carrier accumulation. Since the free carrier change in the bulk region is barely noticeable when compared to the accumulation region, the electro-optic effect is mainly determined by the carrier accumulation region of 1 nm thickness [18]. In practice, since extremely high electric field can be applied across the HfO<sub>2</sub> layer under a moderate bias voltage, the electrical breakdown in the dielectric layer may limit the maximum amount of charge accumulation. According to our analysis, the maximum electric field across the 5-nm-thick HfO<sub>2</sub> layer at 10 V bias is about 13 MV/cm in our design, and it is lower than a reported break down field of 15~40 MV/cm [31]. In the literature, the interface quality of both metal and silicon side is believed to be an important factor to obtain a high dielectric strength of HfO<sub>2</sub>.

Meanwhile, it is well known that the optical property of the ITO material closely follows the Drude model,  $\epsilon(\omega) = \epsilon_\infty - \omega_p^2 / (\omega^2 + i\omega\Gamma)$ , where  $\epsilon_\infty$  is the background permittivity,  $\omega_p$  the plasma frequency,  $\omega$  the angular frequency, and  $\Gamma$  is the collision frequency. Several previous papers have calculated the permittivity of ITO using the experimentally measured reflectance and transmittance, and we choose a fitting result of Michelotti *et. al* ( $\epsilon_\infty = 3.9$  and  $\Gamma = 2.9 \times 10^{15} \text{ s}^{-1}$ ) [9, 10]. The plasma frequency  $\omega_p = (N_0 e^2 / \epsilon_0 m_{eff})^{0.5}$  is mainly determined by the ITO doping concentration,  $N_0$ , which is in the range of  $10^{19} \sim 10^{21} \text{ cm}^{-3}$  depending on the deposition conditions, defect states, and film thicknesses [22]. In this paper, we consider that the doping is  $N_0 = 3 \times 10^{19} \text{ cm}^{-3}$ .

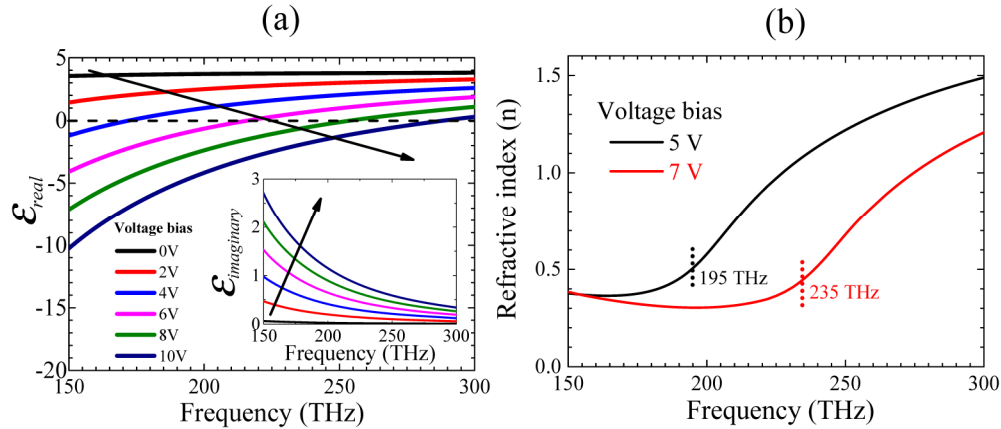


Fig. 3. (a) The real part of the ITO permittivity as a function of the operational frequency in the ITO accumulation region. The inset shows the imaginary part of the ITO permittivity. The horizontal dashed line indicates an ENZ regime. The arrows represent a direction in which a voltage bias increases. (b) Refractive index of the ITO's accumulation layer for the 5 and 7 V bias. The two vertical dashed lines indicate the ENZ frequencies at each voltage.

Based on the average electron densities with different voltage biases shown in Fig. 2(b), the complex permittivity and the refractive index values of the ITO layer are plotted at the near-infrared wavelengths in Fig. 3. It can be seen that a crossover frequency on which a real part of the permittivity becomes zero increases with the input bias voltage. This point is commonly referred to as an ENZ frequency. In fact, the absolute value of the permittivity does not become zero due to the non-zero imaginary part. As shown in the inset of Fig. 3(a), the imaginary part of the permittivity, which is related to the optical loss, grows with the voltage bias. Larger free carrier concentrations make the ITO's optical property more metallic, and the accumulation layer becomes more lossy at the optical frequency range. Despite the absorption losses from the non-negligible imaginary part, the ENZ frequency plays an important role in the phase evolution within the modulator device. Moreover, it is important to note that the refractive index changes in the unity order depending on the voltage bias as shown in Fig. 3(b) [32]. This significantly affects the effective modal index of the slot waveguide modulator, and results in phase modulation. In the later sections, we will explain the detailed modulation mechanism in terms of the ENZ effects and ITO's optical properties.

#### 4. Modulation operation

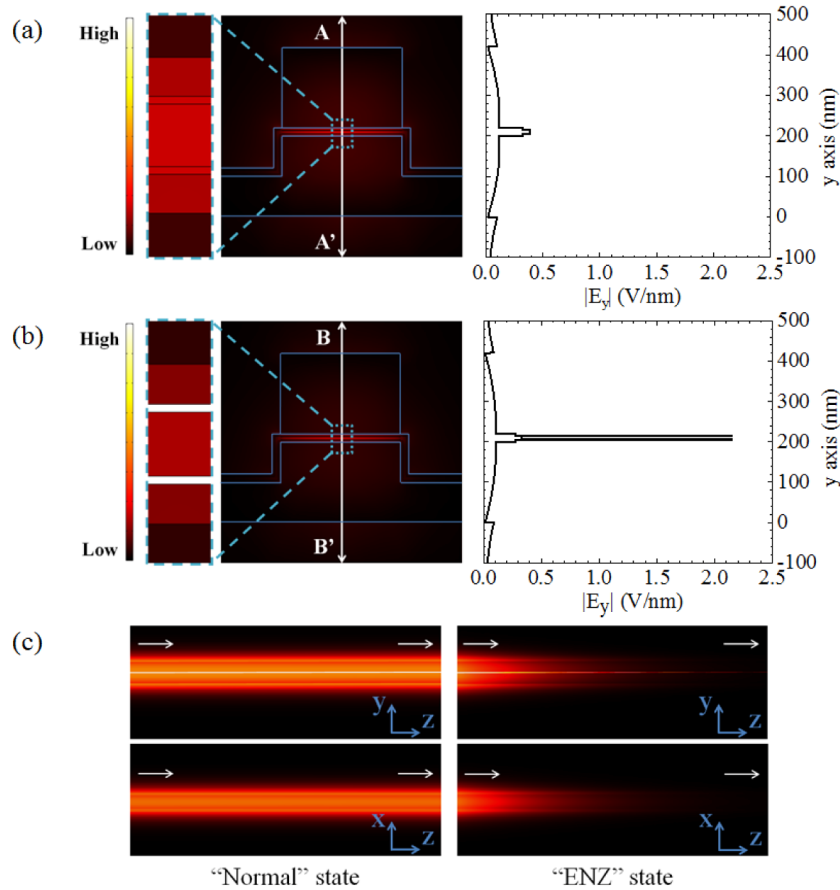


Fig. 4. Electric field intensity profiles at the wavelength of 1550 nm (xy plane), and the absolute values of  $E_y$  along the white lines (A-A' and B-B'). (a) A TM mode profile at the "normal" state with 0 V bias. (b) A TM mode profile at the "ENZ" state with 5 V bias. Dashed rectangles illustrate the magnified views of the electric field intensity profiles near the core of the waveguide modulator. (c) The propagating electric field profiles of the "normal" (left column) and "ENZ" (right column) state obtained from 3D FEM simulations.

There exist two fundamental modes with different polarizations at the near-infrared regime for the silicon waveguides and the proposed phase modulators: namely a TE and TM mode. These two modes are supported by both the rib and slot waveguide sections in Figs. 1(b) and 1(c). Since the material layers of the device are vertically stacked, the TM mode experiences tighter light confinement into the active region than the TE mode and is more suitable for the modulation operation. Therefore, we only consider the TM polarization in our computer simulations. As an example, the mode profiles at two different voltage biases (0 and 5 V) are shown in Figs. 4(a) and 4(b). The mode profiles and the corresponding effective mode indices are obtained from a commercial software based on the finite element method (FEM) [33]. In this paper, we define an 'ENZ' and 'normal' state depending on whether a real part of the permittivity for the active region is zero or not. The electric field profiles for the 'ENZ' and 'normal' mode are almost same except for the active carrier accumulation layer. In the case of the 'normal' state, the electromagnetic energy is spread over the whole ITO layer. On the other hand, the electric field for the 'ENZ' mode is intensively concentrated within the accumulation region of ITO with the thickness of  $\lambda_{TF}$ . This physical phenomenon is attributed

to the ENZ effect [14, 15]. Due to the boundary condition, the surface normal component of the electric field can be sharply increased near the active ENZ region, where the permittivity becomes extremely small. As a result, the tightly confined electric field within nanometer-scale accumulation layer allows strong light-matter interactions capable of highly efficient amplitude and phase modulation.

Figures 5(a) and 5(b) plot the effective modal refractive index ( $\beta(V, f)/k_0 = n_{eff}$ ) and the extinction coefficient ( $\alpha(V, f)/k_0 = \kappa_{eff}$ ) for the propagating TM mode in the modulator section at the near-infrared regime with various voltage biases, respectively, where  $k_0$  is the vacuum phase constant. Note that  $\beta(V, f)$  and  $\alpha(V, f)$  are the modal phase and attenuation constant, respectively, and they are the functions of the voltage bias,  $V$ , and the operating frequency,  $f$ . In Fig. 5(b), each curve has an absorption peak centered at the ENZ frequency. As the voltage bias increases, the peak frequency shifts toward a higher frequency and the peak values of  $\alpha$  and  $\kappa_{eff}$  increase. Figure 5(c) represents a mode confinement factor as a function of the operational frequency. The mode confinement factor can be expressed as  $\eta = \int_{ITO_{acc}} W(r)dr / \int_{all} W(r)dr$ , which is the ratio of the electromagnetic energy confined in the accumulation layer of ITO [34, 35].  $W(r)$  is the effective electro-magnetic energy density at a position  $r$ , and given by

$$W(r) = \frac{1}{2} \text{Re} \left\{ \frac{d[\omega \epsilon(r)]}{d\omega} \right\} |E(r)|^2 + \frac{1}{2} \mu_0 |H(r)|^2,$$

where  $|E(r)|^2$  and  $|H(r)|^2$  are the electric and magnetic field intensity, respectively.  $\epsilon(r)$  and  $\mu_0$  are the permittivity and vacuum permeability, respectively. The permittivity values for ITO are obtained from Figs. 3(a)-3(b). The mode confinement,  $\eta$ , gets maximized near the ENZ frequencies and its overall shape is nearly identical to the  $\kappa_{eff}$  curves in Fig. 5(b). This implies that the photons tightly confined within the accumulation layer at the ENZ frequency strongly interact with accumulated electrons and thus are efficiently absorbed with a high modal extinction coefficient. In short, the TM mode characteristics near the ENZ frequencies are largely determined by the optical properties of the ITO's active region. As shown in the Fig. 4(c), we confirm the ENZ effect more clearly through the propagating electro-magnetic wave in the modulator when the voltage bias is on the "normal" or "ENZ" state. Compared to the "normal" state, electric field in the "ENZ" state suffers from high absorption loss. In addition, since a higher voltage bias induces more electrons at the dielectric-ITO interface, the maximum absorption increases with the applied voltage. The combined effect of the higher electron concentration and tighter mode confinement at the accumulation region results in higher absorption peaks in Fig. 5(b).

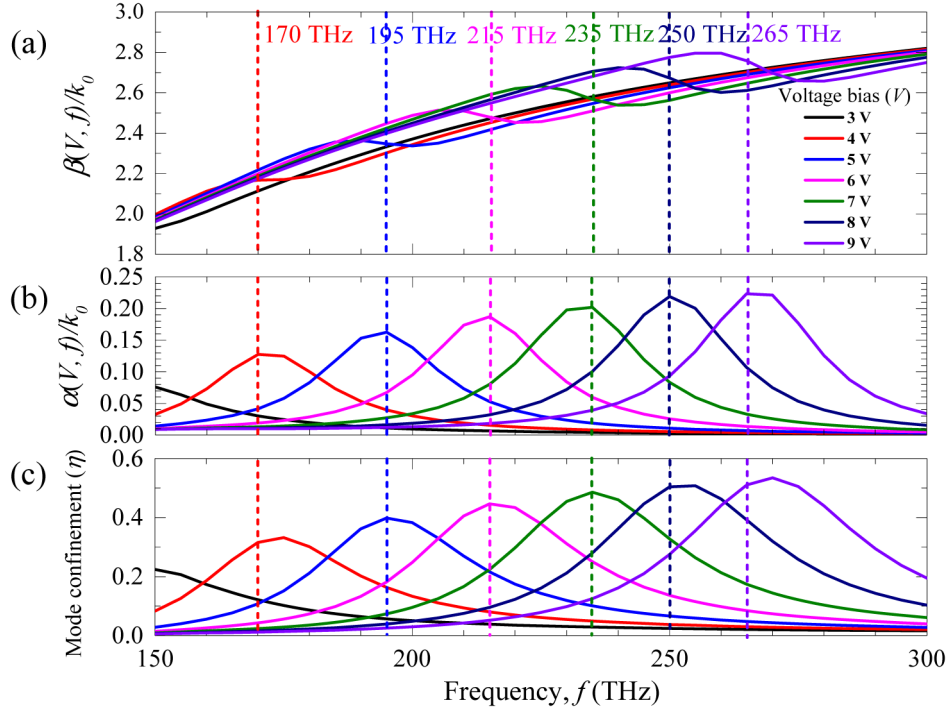


Fig. 5. (a) A real and (b) imaginary part of the effective mode index for the TM mode with respect to the operational frequency. An ENZ frequency for each voltage bias is indicated by the dashed vertical lines with the corresponding color. (c) Mode confinement factor of the ITO's active layer with respect to the operational frequency for various bias voltages.

As mentioned before, the effective modal absorption is mostly affected by the optical properties of the ITO accumulation layer at the ENZ frequency. Most studies with the ITO-based modulators have mainly focused on amplitude modulation between a 'normal' and 'ENZ' mode as discussed in the previous section [14, 15]. However, it should be noted that the TM mode also undergoes dramatic changes of a modal phase constant,  $\beta(V, f)$  near the ENZ point in Fig. 5(a) because the ITO's ENZ phenomena are closely related to electro-refractive modulation as well as electro-absorption modulation [32].

The graphs in Fig. 5 show the feasibility of various phase modulation applications for the digital modulation schemes. For example, the binary phase shift keying (BPSK) modulation format has two different states ('0' and '1') corresponding to a phase shift of 0 and  $\pi$  radians. To support such a BPSK scheme using our device, we can employ a modulation mechanism similar to the phase modulation from a microring resonator as previously reported in [21, 36]. A proper shift of the ENZ frequency and the effective modal index can generate a significant phase change while maintaining the output amplitude level unchanged. Figure 5(a) shows that the modal refractive index,  $\beta(V, f)/k_0$ , is sharply altered near the ENZ frequency, resulting in a significant phase shift for the propagation mode in the frequency range between the two ENZ frequencies at different voltages. The electro-refractive modulation can be explained by two main factors: a mode confinement factor and the optical material properties of the active layer. As shown in Fig. 5(c), the mode confinement factor of the active layer is maximized at the ENZ frequency. At those points, the refractive index of the accumulation layer becomes much lower than those of the surrounding materials as shown in Fig. 3(b), resulting in sharp decrease of the slope in the effective modal index-frequency diagram in Fig. 5(a).

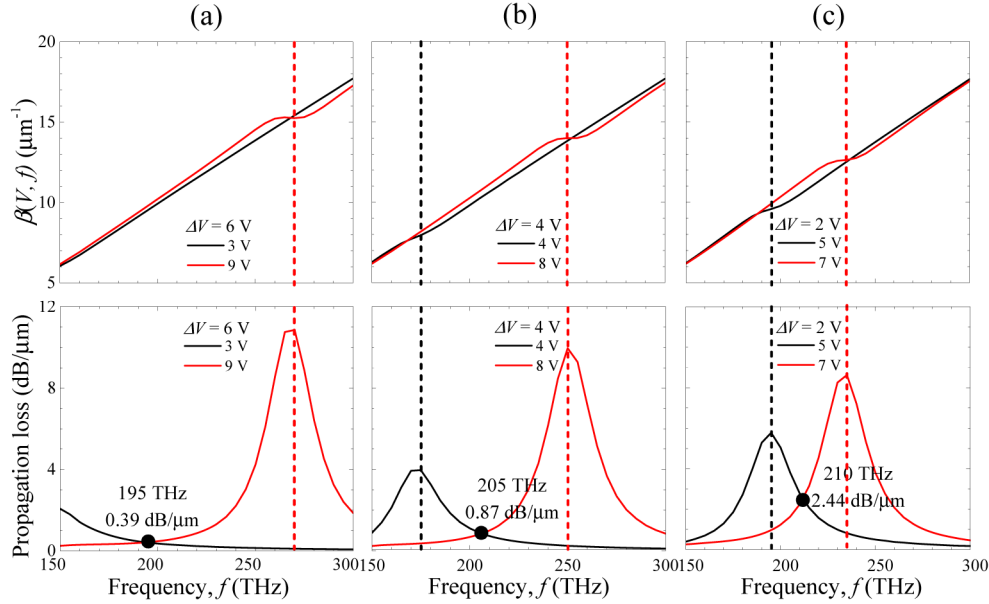


Fig. 6. Dependence of a phase constant ( $\beta(V, f)$ ) and propagation loss on the operational frequency. The dc voltage bias,  $V_{dc}$ , is fixed to 6 V. The graphs show phase modulation operation when the voltage swing  $\Delta V$  is (a) 6 V, (b) 4 V, (c) 2 V, respectively. Dashed red and black vertical lines represent an ENZ frequency for the corresponding input voltage. The black dots indicate the crossover points where the propagation losses become equal for two different input voltages.

Figure 6 illustrates the digital phase modulation schemes with different voltage swings. By appropriately adjusting the modulator length,  $L_{modulator}$ , a  $\pi$  radian phase shift can be achieved. When a central dc voltage bias is fixed at  $V_{dc} = 6$  V, the modulator length for a  $\pi$  phase shift ( $L_{\pi}$ ) is calculated to be  $11.8 \mu\text{m}$  ( $\pi/(\beta(9 \text{ V}, 195 \text{ THz}) - \beta(3 \text{ V}, 195 \text{ THz}))$ ), Fig. 6(a),  $6.8 \mu\text{m}$  ( $\pi/(\beta(8 \text{ V}, 205 \text{ THz}) - \beta(4 \text{ V}, 205 \text{ THz}))$ ), Fig. 6(b)), and  $4.2 \mu\text{m}$  ( $\pi/(\beta(7 \text{ V}, 210 \text{ THz}) - \beta(5 \text{ V}, 210 \text{ THz}))$ ), Fig. 6(c)) at the various voltage swings and frequencies. These results show that a relatively small voltage swing is required to achieve the  $\pi$  phase shift within a short propagation length. In addition, the required  $\pi$  phase shift length of the modulator is extremely small when compared to the silicon p-n or p-i-n junction-based phase shifters [3, 5]. In the case of the 6 V swing, our modulator has a decent modulation efficiency of  $V_{\pi}L_{\pi} \sim 0.0071 \text{ V}\cdot\text{cm}$ , where  $V_{\pi}$  is the voltage swing required for a  $\pi$  radian phase shift. Given that the typical modulation efficiency of silicon-based waveguide modulators is in the range of  $0.01 \sim 1 \text{ V}\cdot\text{cm}$ , the proposed device has a great potential for high-density optoelectronic integrated circuits.

Another important parameter related with phase modulation is the optical loss from propagation attenuation. As shown in Figs. 6(a)-6(c),  $\pi$  phase shift without output amplitude variation for the BPSK modulation scheme can be achieved at a point where two bell-shaped propagation loss curves intersect with each other. The corresponding loss for the device is given by  $20(\log_{10}e) \times \alpha(V, f) \times L_{modulator}$ . For example, the propagation loss for the phase modulator operating at the 195 THz input optical frequency is calculated to be 4.60 dB ( $(8.68\pi\alpha(9 \text{ V}, 195 \text{ THz})/(\beta(9 \text{ V}, 195 \text{ THz}) - \beta(3 \text{ V}, 195 \text{ THz})))$ ). Since  $\alpha(3 \text{ V}, 195 \text{ THz}) = \alpha(9 \text{ V}, 195 \text{ THz})$  as shown in Fig. 6(a), the output signals for the 3 V and 9 V modulator biases experience the same amount of attenuation at the 195 THz input frequency, while their output phases differ by  $\pi$ . It is necessary to control the input voltage precisely to obtain phase-only modulation with minimal intensity fluctuation. It should also be noted that the propagation

attenuation for the  $\pi$  phase shift increases with the operational optical frequency as indicated in Fig. 6.

## 5. Discussion

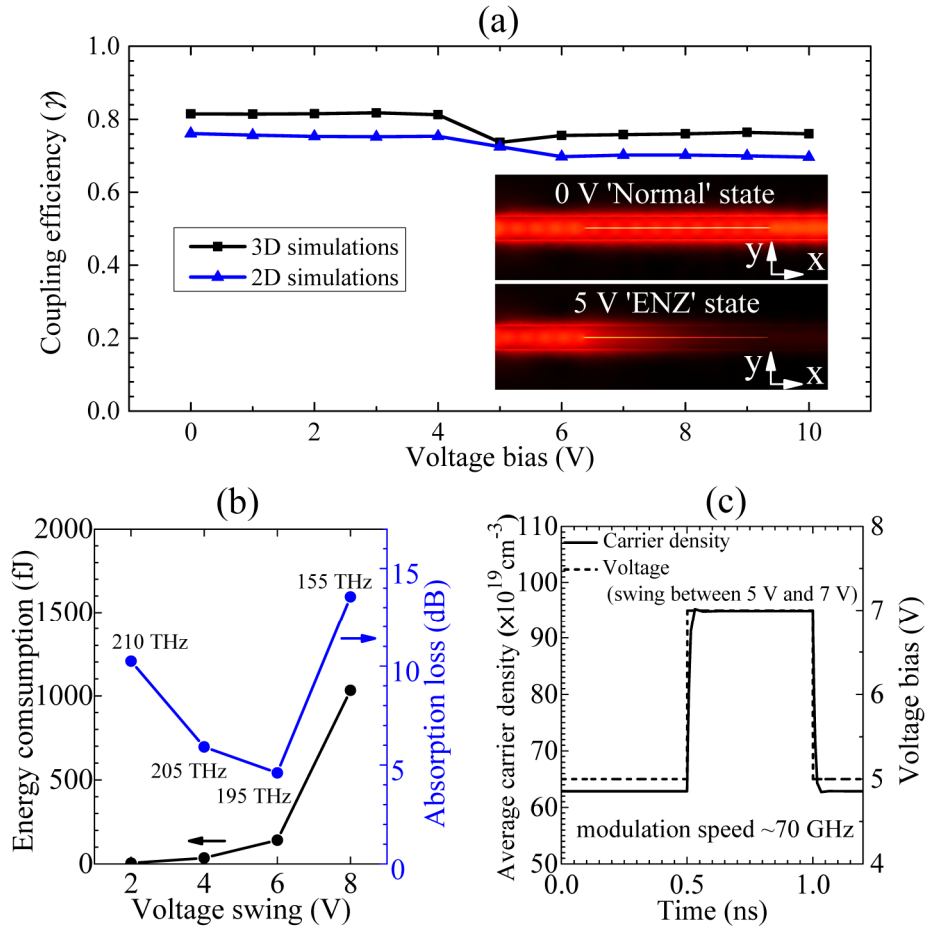


Fig. 7. Simulation analysis of the modulation performance. (a) Mode coupling efficiency between a silicon rib waveguide and modulator depending on the voltage biases at 1550 nm. The inset figures show 3D propagation profiles for a 'normal' and 'ENZ' state in the modulator (a silicon\_waveguide/ITO\_modulator/silicon\_waveguide structure). (b) Dependence of energy consumption per bit and propagation loss as a function of the voltage swing for  $\pi$  radian phase shift ( $L_{\text{modulator}} = L_{\pi}$ ). The dc voltage bias is fixed at  $V_{dc} = 6 \text{ V}$ . (c) Transient analysis of the average electron density in the ITO accumulation region. This transient graph represents a case with a voltage swing of  $\Delta V = 2 \text{ V}$  and a dc voltage of  $V_{dc} = 6 \text{ V}$ .

The important parameters that determine the modulation performance of the proposed device include the coupling efficiency with an input/output silicon waveguide, modulation speed, and energy consumption. First of all, high coupling efficiency over the broad frequency range is necessary to minimize the device's insertion loss and to obtain good modulation efficiency. 2D FEM simulations are performed to find out the fundamental TM modes in the silicon waveguide and modulator at the wavelength of 1550 nm. For 2D mode analysis, the coupling efficiency between the two modes can be obtained from a mode overlap integral over the 2D cross-sectional areas, which is given by

$$\gamma = \frac{\left| \iint E_{\text{waveguide}}(x, y) E_{\text{modulator}}^*(x, y) dx dy \right|^2}{\iint |E_{\text{waveguide}}(x, y)|^2 dx dy \iint |E_{\text{modulator}}(x, y)|^2 dx dy},$$

where  $E_{\text{waveguide}}$  and  $E_{\text{modulator}}$  indicate the electric field distribution for the fundamental TM mode of the silicon rib waveguide and modulator in Figs. 1(b)-1(c). For 3D FEM simulations, the same mode overlap integral equation is applied for estimating the coupling efficiency at the interfaces between the input/output silicon waveguide and the proposed modulator. As shown in Fig. 7(a), the coupling efficiency decreases around a 5 V bias for both 2D and 3D simulations due to the highly confined electric field in the ITO's accumulation region at the 'ENZ' state. Although the coupling efficiency slightly depends on the voltage bias, it is maintained within the range of 70~80% regardless of the simulation methods. This implies that a mode mismatch between a silicon rib waveguide and the modulator is sufficiently low over the wide range of the voltage bias.

Low energy consumption is another important factor which affects the overall modulation performance. To estimate the average energy efficiency for digital phase modulation, we apply a dynamic energy consumption equation of  $C(\Delta V)^2/4$  [11], where  $C$  is the capacitance for the device and  $\Delta V$  is the voltage swing. The values of  $C$  are obtained by multiplying  $C_{1\mu\text{m}}$  ( $\sim 1.3$  fF/ $\mu\text{m}$ ) and  $L_\pi$  where  $C_{1\mu\text{m}}$  is the capacitance per unit length directly extracted from the electrical simulation [25]. Figure 7(b) represents the dependence of the energy consumption and propagation loss on the voltage swing for the  $\pi$  phase shift when the dc voltage bias ( $V_{dc}$ ) is 6 V. As expected, the required energy increases with the voltage swing. In addition, the propagation loss monotonically decreases in the range of 2 and 6 V because the absorption loss per unit length gradually decreases as mentioned in the previous section. However, the propagation loss sharply increases again when the voltage swing increases further to 8 V. In this case, the  $\pi$  phase shift length ( $L_\pi$ ) becomes too long, and the confined light loses most of its energy as it propagates through the modulator's length of  $\sim 50$   $\mu\text{m}$ . Small energy consumption below 100 fJ/bit for future optical interconnect applications [37] can be achieved by a small voltage swing of  $\Delta V \sim 4$  V with a relatively low propagation loss ( $\sim 6$  dB) and a short modulation length (6.8  $\mu\text{m}$ ).

When there is no other external resistance and capacitance, an RC time constant typically limits the cutoff frequency and 3 dB modulation bandwidth. The internal resistance can be estimated from the resistivity of silicon and ITO as well as the modulator length. Assuming the p-type Si (doping concentration of  $5 \times 10^{17}$   $\text{cm}^{-3}$ ) and ITO resistivity of  $5 \times 10^{-2}$   $\Omega \cdot \text{cm}$  and  $5 \times 10^{-4}$   $\Omega \cdot \text{cm}$ , respectively [27], the estimated device resistance is about 79  $\Omega$  for the device length of 4.2  $\mu\text{m}$ . Considering the above-mentioned capacitance ( $C = \sim 5.6$  fF for 4.2  $\mu\text{m}$  modulation length), the estimated RC-limited frequency is about 360 GHz. Meanwhile, Fig. 7(c) shows the transient analysis result for the electron density in the accumulation region of ITO obtained from the electrical simulation [25]. Notice that the modulation speed for the 2 V swing is about 70 GHz. It is shown that the modulation speed is affected by the low mobility of ITO rather than a RC time constant because high doping of ITO and strong electric field across the HfO<sub>2</sub> layer lowers the mobility of degenerate semiconductors. Nevertheless, the estimated device speed is sufficiently high for the integrated optical circuit applications [1].

## 6. Conclusion

In summary, an electro-optic phase modulator based on a silicon slot waveguide with ITO is proposed. The device consists of two vertically stacked silicon layers and a core with ultrathin HfO<sub>2</sub>/ITO/HfO<sub>2</sub> multilayers. Due to the refractive index difference between core materials and silicon, the electro-magnetic field can be tightly confined in the active material. When an external voltage bias is applied between the ITO thin film and the silicon layer, electron accumulation layers are formed, resulting in the epsilon-near-zero effect which

contributes to phase and amplitude modulation. With a voltage swing of as low as 2 V, the modulator experiences a large variation of the effective mode index, causing a  $\pi$  radian phase shift within the device length of  $<10 \mu\text{m}$  at 210 THz according to our computer simulations. The maximum modulation speed is estimated to be about 70 GHz, and the energy consumption of the device can be below 100 fJ/bit with an optimized voltage bias. The proposed amplitude-phase modulator has a variety of merits in respect to its ultra-compactness, high power efficiency, and wide bandwidth for future on-chip optical communication modules and optoelectronic integrated circuits.

#### **Acknowledgment**

This work was supported by the Center for Integrated Smart Sensors funded by the Ministry of Science, ICT & Future Planning as Global Frontier Project (CISS-2012M3A6A6054191).